

Towards adaptive drag reduction of a flat-back 3D bluff body in variable pitch and crosswind by flow orientation at the base separation

Y. Fan · V. Parezanović · S. Fichera · O. Cadot

Received: date / Accepted: date

Abstract The sensitivity of the drag to the rear design of a flat-back body is investigated under different body attitudes defined by the pitch ($-1.5^\circ, 0^\circ, +1.5^\circ$) and yaw (up to 15°). The rear design consists of taper angles at the top and bottom trailing edge varying from 0° (no taper) to 12.5° . Compared to the fixed optimal rear design that minimizes drag at the wind-aligned body attitude, the rear design adaptation to the change of attitude produces a noticeable drag reduction up to 5% depending on the pitch angle within a yaw range smaller than 2° . It is shown that this drag reduction is related to the vertical wake steady instability interfering with the rear design. For yaw larger than 2° and up to 12° , an almost constant drag reduction of 2% is found and shown to be a compromise between a beneficial pressure recovery on the flat base and a detrimental pressure drag on the tapers. At larger yaw angles and whatever the pitch angle is, there is no compromise anymore such that any taper angle different from 0° produces a drag increase leading eventually to the squareback rear design as the optimal design. Overall, the study emphasizes the potential of adaptive control of the top and bottom trailing edge tapers to arbitrary body attitude even at small yaw angles when the pitch is varied.

1 Introduction

The increase of global transportation (such as aviation, shipping and road transportation) has greatly exacerbated the environmental issues. Out of the latter three, ground vehicle transportation leads to more than 70% of greenhouse gas emissions. Within this large contribution, the resistance force of the air flow past vehicles has been identified as the most important source of emission in highway cruise operating conditions; thus obliging engineers and researchers to mitigate the harmful emissions by optimizing the aerodynamic performance of vehicles.

Fundamental research on ground vehicle aerodynamics focuses on simplified three-dimensional (3-D) bluff bodies. For blunt trailing edge bodies (mimicking minivans, sport utility cars and lorry trailers), the main source of aerodynamic drag has been identified as the low pressure at the base (also called base drag or suction) due to the massive separation at the trailing edge ([Ahmed et al., 1984](#)). Passive techniques to reduce this base drag have thus been investigated, with a specific attention to small modifications in order to be considered by the car manufacturers. Since the work of [Wong and Mair \(1983\)](#), it is known that a substantial drag reduction can be obtained with short boat-tailing. A single taper at the top trailing edge leads to a drag reduction up to 4% for the Windsor model ([Littlewood and Passmore, 2010](#)). This result can be improved to 7% using tapers on both top and bottom sides ([Perry et al., 2015, 2016](#)). It is nowadays very common to observe sport utility cars and minivans equipped at the base with a top spoiler

Y. Fan · O. Cadot · S. Fichera
School of Engineering, University of Liverpool,
Liverpool L69 3GH, UK

V. Parezanović
Aerospace Engineering Department, Khalifa University
of Science and Technology,
Abu Dhabi, UAE
E-mail: Yajun.Fan@liverpool.ac.uk

and a bottom diffuser angle revealing the effort made by the manufacturer to reduce drag.

However, these optimal strategies may lose their efficiency when the body attitude changes. It has been recently pointed out by [Howell \(2015\)](#) that real driving conditions, such as the different attitudes of the vehicle produced by crosswinds (equivalently yaw), must also be considered. Similarly, pitch variations (due to different front/rear mass loading) have been shown by [Bonnavion et al. \(2019\)](#) to affect the drag of minivans, albeit to a lesser degree.

An extensive investigation by [Howell \(2015\)](#) on a series of different types of real cars recalls that the drag rises with yaw significantly, often referred to as an induced drag effect. The drag increase with yaw is also generic to simplified 3-D bluff bodies ([Hassaan et al., 2018](#); [McArthur et al., 2018](#); [Howell, 2015](#); [Gohlke et al., 2007](#)). There is no universal behaviour for the drag variation with yaw which can be either linear or polynomial depending on the shape of the body ([Gohlke et al., 2007](#); [Grandemange et al., 2015](#); [Bello-Millán et al., 2016](#)). As atmospheric crosswinds are unavoidable on real road conditions, [Howell et al. \(2018\)](#) proposed that aerodynamic performance of ground vehicles should take into account nonzero yaw angles. The concept of a wind-averaged drag coefficient (see [Cooper 1976](#); [Ingram 1978](#)), denoted C_{DWC} is thus derived by using a wind speed distribution representative to the geographic region. This distribution is sampled into four probabilities: a_{0° , a_{5° , a_{10° and a_{15° , each being related to their respective yaw angle, and also depending on the wind speeds of the different countries. The wind-averaged drag coefficient is simply the weighted average defined as $C_{DWC} = a_{0^\circ}C_x^{0^\circ} + a_{5^\circ}C_x^{5^\circ} + a_{10^\circ}C_x^{10^\circ} + a_{15^\circ}C_x^{15^\circ}$ where C_x^β is the drag coefficient at yaw β .

In addition to the generic induced drag effect with yaw, some severe wake transitions can occur at yaw leading to further drag increase as reported for real cars by [Bonnavion et al. \(2017\)](#). The transition can have a different origin, either associated with an intermittent reattachment on the slanted rear window (also reported for an Ahmed body with a 35° slant angle by [Meile et al. 2016](#)) or a wake transition due to the steady wake instability (firstly reported for a squareback Ahmed body by [Grandemange et al. 2013a](#)). While the reattachment on the rear slant could be rare as it requires a large yaw angle (about 10° or more), the latter due to the steady wake instability occurs at

few degrees only. Later, [Bonnavion et al. \(2019\)](#) made a thorough study changing the pitch and the clearance in addition to the yaw on a series of real minivans with rotating wheels and road effect. They found sharp transitions of the wake orientation in the vertical direction varying the clearance and the pitch at null yaw that they associated with the steady instability and recovered the transition at small yaw angle observed by [Bonnavion et al. \(2017\)](#) but with another vehicle type.

The observations from real car aerodynamics motivated the fundamental study of [Fan et al. \(2022\)](#). They performed parametric studies in pitch, yaw and clearance of a taller than wide squareback Ahmed body known to be subjected to the steady instability with wake orientation in the vertical direction as observed for the real minivans above. They identified wake transitions with bistable dynamics within very specific regions of the parametric pitch/yaw space as well as in the clearance/yaw space thus generalizing with an Ahmed body the few transitions of [Bonnavion et al. \(2019\)](#) observed with real minivans by changing their attitude.

The recent theoretical effort of [Zampogna and Boujo \(2023\)](#) elucidates the origin of the steady instability. In the absence of a ground proximity, it shows that for a Reynolds number of few hundreds (depending on the forebody geometry and body length), the wake of a prism loses the symmetry of the geometry and encompasses a pitch-fork bifurcation towards a deviated wake defining the steady global instability. The deviation occurs in the direction of the major axis of the rectangular base resulting in a permanent asymmetry in that same direction. There are two possible deviations of opposite signs, the so-called P and N states. This bifurcation has been reported experimentally ([Grandemange et al., 2012](#)) and numerically ([Evstafyeva et al., 2017](#)) before this theoretical work.

The yaw effect has been recently considered in the research related to drag reduction; an overall improvement of 3% for the wind-averaged drag coefficient can be achieved through the variable rear design. Variable angles for flaps ([Garcia de la Cruz et al., 2017](#)) or tapers ([Varney et al., 2018](#)) on both sides can achieve a better drag reduction at non-zero yaw angles, compared to that of a static design which has been optimized for wind-aligned body attitude. In the work of [Urquhart et al. \(2020b\)](#), the base cavity with nine flaps located at its trailing edge achieved a 2% decrease

in drag at yaw compared to the cavity without flaps. The angles of the flaps were optimised from experimental data using a surrogate model-based algorithm (Urquhart et al., 2020a).

While these studies focus on adaptive lateral flow orientation with yaw, to our knowledge, there are no investigations of adaptive flow orientation at the top and bottom trailing edges with yaw and pitch. These are actually of a great practical interest since top spoilers and bottom diffusers are commonly used to reduce the drag of real-world cars. In addition, the existence of the wake steady instability in the vertical direction, revealed by Bonnavion et al. (2019) for minivans, emphasizes the potential sensitivity of the drag to the pitch attitude. To that aim, the present paper attempts to evaluate the potential of an adaptive control to reduce the drag under variable driving conditions for a flat-back Ahmed body subjected to the steady wake instability in the vertical direction. This potential is investigated with variable body attitudes (pitch and yaw) likely to happen in real-world conditions.

The paper is organised as follows. The experimental set-up is described in the next section §2 giving details about the model and the facility (§2.1), the variable rear designs (§2.2) and the measurements techniques (§2.3). Section §3 introduces the experimental protocol (§3.1) and a drag decomposition (§3.2) to obtain and analyse the results presented and discussed in §4. This section is split into 4 parts, the rear design that minimises the drag at wind aligned flow condition (called the reference design) is first studied and compared in §4.1 to the aerodynamic properties of the square-back geometry. Parts §4.2 and §4.3 attempt to synthesize the main flow and drag characteristic when both the rear design and the body attitude are changed. The last part §4.4 study and discuss the best design at each attitude, or equivalently the performance improvement of an adaptive design compared to a fixed design. The results are finally concluded in §5.

2 Experimental Set-up

2.1 Model geometry and facility

The considered geometry is a flat-back Ahmed model (see Fig. 1) with dimensions $L = 560$ mm, $W = 180$ mm, and $H = 200$ mm. It corresponds to a 1:2 scale of the original Ahmed et al. (1984)'s body design. However, the rectangular base is

taller than wide with an aspect ratio of $H/W = 1.11$ to have the steady instability in the vertical direction. This aspect ratio has been chosen following the recommendations in Grandemange et al. (2013a) and the corresponding steady instability for this geometry has been recently studied by Fan et al. (2022) with variable attitudes. The body is supported by four cylinders of 15 mm in diameter, leaving a ground clearance $C = 25$ mm at mid-distance between the front and rear axle (or cylindrical supports) as shown in Fig. 1(a). The model is placed on two motorized elevators (Standa 8MVT100-25-1), to independently control the clearance of the front and rear axles, leading to the variation of the pitch angle α , while keeping the mid-distance ground clearance constant at $C = 25$ mm. This assembly is mounted on a motorized rotation stage (Standa 8MR190-90-59) driven by a motorized rotation stage to control the yaw angle β with a precision of 0.02° . The positive direction of the pitch and yaw are defined as shown in Figs. 1(a, b).

The experiment is conducted in an open circuit blow-down wind tunnel. Air is blown downstream by a fan located upstream of a section of 9:1 contraction ratio and the test section. The test section dimension is 1.2 m-wide by 0.6 m-high and 2.4 m-long. The static pressure of the free-stream p_∞ is measured with two Pitot tubes at the inlet of the test section, one on both sides to compensate for pressure adjustment when the body is at yaw, and the static pressure is given by their mean. The free-stream turbulent intensity is 1% and with the model, the blockage ratio 4.9%. The velocity is set to $U_\infty = 15.8$ m/s (i.e. the dynamic pressure $q_\infty = 150$ Pa), corresponding to the Reynolds number $Re = U_\infty H/\nu \approx 2.1 \times 10^5$. The height of the body H and the free-stream velocity U_∞ are chosen as length and velocity scaling units respectively.

2.2 Rear designs

As can be seen in Fig. 1(c), the afterbody is equipped with removable top and bottom parts where interchangeable modules of different slant angle can be fitted. Each module has dimensions of $L_m \times h_m = 70$ mm \times 40 mm with the slant starting at $l_m = 40$ mm. A combination of top, φ_t and bottom φ_b angles are referred to as a "rear design". There are 6 different tapered modules (0° , 2.5° , 5° , 7.5° , 10° , 12.5°) for the top and bottom trailing edges leading to 36 different rear designs (φ_t, φ_b).

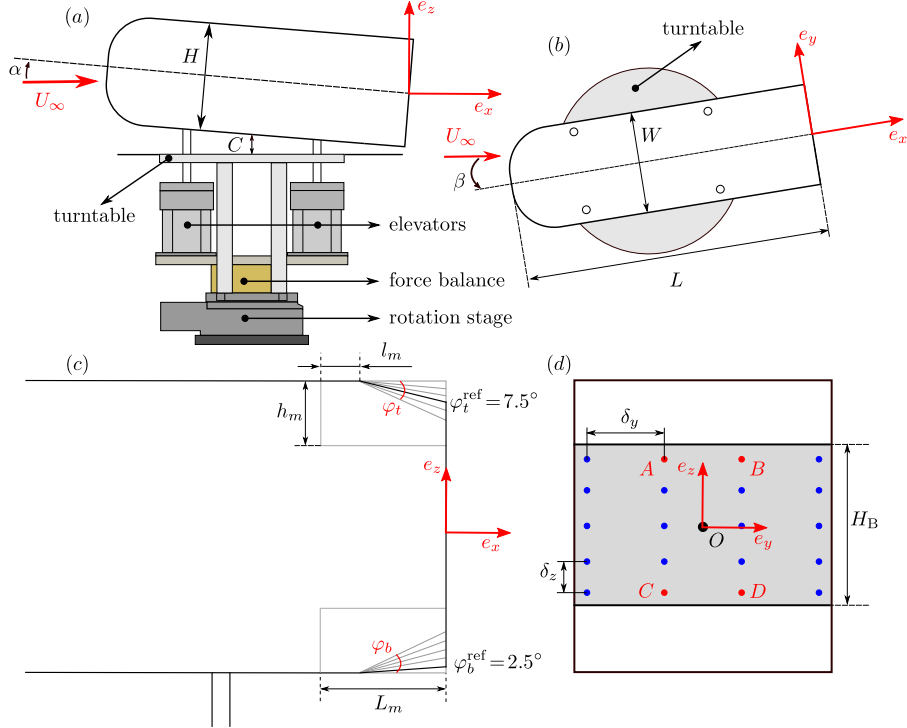


Fig. 1: Sketch of the experimental apparatus: side (a), and top (b) views of the model showing the attitude setting system and the force balance. Side (c) and rear (d) views of the afterbody geometry. Annotated angles in (c) correspond to the reference design. Blue and red dots in (d) indicate pressure taps, where four (A, B, C, D) are used to calculate the base pressure gradient (see text).

The rear design ($\varphi_t^{\text{ref}}, \varphi_b^{\text{ref}}$) having the lowest drag when the body is positioned at wind-aligned attitude ($\alpha = \beta = 0^\circ$) defines the reference design. In the following, we will assess the impact of varying pitch, yaw and rear designs on the body aerodynamics with respect to this reference design.

2.3 Aerodynamic force and pressure measurements

A six-component force balance (F/T Sensor: Gamma IP65, manufactured by ATI Industrial Automation) is supporting the two elevators and rotates with the rotary stage. It measures f_x, f_y, f_z in the coordinates system ($\mathbf{e}_x, \mathbf{e}_y, \mathbf{e}_z$) of Fig. 1(a, b). Time series of the components are acquired at a sample frequency of 1 kHz. The model frontal area $S = H \times W$ is used to calculate the force coefficient components:

$$c_i = \frac{f_i}{q_\infty S}, (i = x, y, z). \quad (1)$$

where q_∞ is the dynamic pressure. The manufacturer force balance resolution is 0.025 N for f_x, f_y , and 0.05 N for f_z which, given the flow velocity U_∞ translate to 5×10^{-3} for c_x, c_y and 10×10^{-3} for c_z . Feedback from the force balance results shows a better resolution than that of the manufacturer which has been checked through calibrated mass weight measurements in the x component to be better than 0.005N, say 0.001 in drag coefficient.

Pressure is measured with a Scanivalve ZOC33/64PX pressure scanner placed inside the body. The sampling frequency is 1 kHz per channel with an accuracy better than ± 0.5 Pa on converged mean values (see Fan et al. 2022 for further details). The static pressure p_∞ of the test section is used to compute the instantaneous pressure coefficient:

$$c_p = \frac{p - p_\infty}{q_\infty} \quad (2)$$

Given the flow velocity U_∞ , the measurement uncertainty on the pressure coefficient is ± 0.005 .

There are 20 pressure taps, all located at the base in the space of height $H_B = \frac{3}{5}H = 120$ mm

displayed by the grey area in Fig. 1(d) between the top and bottom removable tapered modules. They give an estimate of the base suction over the grey surface in Fig. 1(d) of dimension $\frac{3}{5}H \times W$:

$$c_B = -\frac{1}{20} \sum_{i=1}^{20} c_{pi}, \quad (3)$$

whose contribution to the total drag coefficient c_x as defined in Eq. 1 is

$$c_{Bx} = \frac{3}{5}c_B, \quad (4)$$

Note that ideally, the pressure force acting on the total vertical blunt base (from the top taper trailing edge to the bottom one) would have been more useful. However it accounts for additional areas of the interchangeable modules which have not be equipped with pressure taps. To be rigorous, we have thus preferred to introduce in the drag decomposition discussed in §3.2 the force on the grey area that is correctly measured instead of the force on the total blunt base that is partially measured. The four pressure taps (A, B, C, D) in figure 1(d) are used to compute the base pressure gradient components:

$$\begin{aligned} g_y &= \frac{(c_p(B) + c_p(D)) - (c_p(A) + c_p(C))}{2\delta y/H} \\ g_z &= \frac{(c_p(A) + c_p(B)) - (c_p(C) + c_p(D))}{8\delta z/H}. \end{aligned} \quad (5)$$

As previously shown by Grandemange et al. (2013b), they are appropriate indicators of the wake orientation and dynamics.

A specific notation is used in the paper for statistical quantities. A temporal average of any quantity denoted by a lower case letter such as a is denoted with a uppercase letter $A = \bar{a}$, and its characteristic fluctuation (or standard deviation) with $\delta A = \sqrt{(a - \bar{a})^2}$. For instance, the mean of g_z is G_z and its fluctuation δG_z .

3 Methodology

This section first presents the experimental protocols to obtain measurements for different body attitudes and rear designs. A drag decomposition is then proposed using the two independent information about the pressure at the base and the total drag, with the idea to estimate the drag force contribution introduced by the top and bottom interchangeable modules of the rear design.

3.1 Measurements at different body attitudes and rear designs

Three different pitch angles are investigated; nose-down at $\alpha = -1.5^\circ$, $\alpha = 0^\circ$ and nose-up at $\alpha = 1.5^\circ$. These extreme values have been chosen from a real life example. We have checked with a real-world Peugeot partner that a variation of 1° in pitch can be obtained with different loads of people either at the front or at the rear, and that the nose-up pitch may be further increased with boot loading. For each pitch, the body is yawed from $\beta = -15^\circ$ to $\beta = 3^\circ$ with a step of $\delta\beta = 1^\circ$ leading to 19 distinct yaw angles. We took advantage of the measurements that have been checked to be symmetric with yaw to limit the exploration towards positive values to 3° . In total, 57 attitudes (α, β) are investigated. For each of the 36 rear designs (φ_t, φ_b) that are manually fitted, the aerodynamic force and the base pressure distribution are recorded for the 57 body attitudes using an automated displacement system. The experimental technique used to avoid the force balance drift during the total duration of the automated experiment is fully described in Fan et al. (2022). The acquisition time for each attitude is 50 s ensuring a good convergence of the mean values as shown in Fan et al. (2022). The automated experiment over the 57 attitudes takes approximately 1 hour. The same experiment is repeated with no wind and subtracted from the wind experiment to suppress the gravity load due to attitude variations.

3.2 Drag decomposition

Both measurements of drag force and pressure at the base are used to formulate a decomposition of C_x into two parts:

$$C_x = C_{Bx} + C_{Rx}, \quad (6)$$

The first contribution C_{Bx} is the drag of the grey area in Fig. 1(d) (as defined in Eq. 4). The second remaining contribution C_{Rx} is the sum of the drag exerted on the top and bottom tapered modules of dimensions $h_m \times L_m$ shown in Fig.1(c), the forebody and the supports.

In order to distinguish between the different model geometries, superscript j will refer to values obtained with a given rear design such as the squareback geometry for $j = 0$, the reference geometry for $j = \text{ref}$ and optimal designs for $j = \text{opt}_{C_x}$ or $j = \text{opt}_{C_{Bx}}$ whether it is the drag or base drag that is minimum.

The drag variation for a model with the rear design (φ_t, φ_b) from the reference model having the same attitude but with the fixed rear design $(\varphi_t^{\text{ref}}, \varphi_b^{\text{ref}})$ reads:

$$\Delta C_x = \Delta C_{Bx} + \Delta C_{Rx}, \quad (7)$$

such that the Δ notation always refers to as a relative variation from the reference model :

$$\begin{aligned} \Delta C_k &= C_k - C_k^{\text{ref}} \\ &= C_k(\alpha, \beta, \varphi_t, \varphi_b) - C_k(\alpha, \beta, \varphi_t^{\text{ref}}, \varphi_b^{\text{ref}}), \end{aligned} \quad (8)$$

where $k = x, Bx, Rx$. With these notations, the drag variation of the squareback geometry compared to the reference design at a given attitude is ΔC_x^0 .

If we reasonably assume that the part due to the forebody and the supports is only a function of the body attitude (α, β) and not of the body rear design (φ_t, φ_b) then ΔC_{Rx} is the drag variation on the slanted modules essentially. Since both variations ΔC_x and ΔC_{Bx} are directly measured, this drag variation is simply assessed as $\Delta C_{Rx} = \Delta C_x - \Delta C_{Bx}$ and will be referred to as the rear design drag variation for the remainder of the paper.

The wind-averaged drag coefficient (Howell, 2015; Varney et al., 2018) is introduced to assess the aerodynamic performance with yaw conditions. It is defined in Varney et al. (2018) as:

$$C_{\text{DWC}} = 0.53C_{x_{\beta=0^\circ}} + 0.345C_{x_{\beta=5^\circ}} + 0.13C_{x_{\beta=10^\circ}}, \quad (9)$$

where the numerical constants are typical to European wind conditions.

4 Results and Discussions

4.1 Reference design

We now consider the fixed rear design called "reference design" that minimizes the drag at the wind-aligned body attitude (i.e. $\alpha = \beta = 0^\circ$). This optimal rear design is obtained for the couple of slant modules $\varphi_t^{\text{ref}} = 7.5^\circ$, $\varphi_b^{\text{ref}} = 2.5^\circ$, achieving a drag reduction of 3.14% compared to the squareback geometry ($\varphi_t = \varphi_b = 0^\circ$). This drag reduction is in-line with the result of Grandemange et al. (2013c), in which they achieved a drag reduction of 3.3% with top and bottom flaps for an optimal design ($12^\circ, 6^\circ$). Further drag reduction can

be achieved using a taper base cavity (Urquhart et al., 2020b), equivalent to flaps on the four trailing edges. The reference rear design is roughly the equivalent of the aerodynamically optimised vehicle commercialised by manufacturers. We recall that measurements on the reference design will be denoted with a "ref" superscript.

Figs. 2(a, b, c) present the aerodynamic drag and its contributions of the reference design as a function of the body attitude. The high sensitivity to the pitch observed below a yaw of 3° is reminiscent of the wake steady instability (Fan et al., 2022), and will be discussed in the last paragraph of §4.1. As expected, the drag coefficient C_x^{ref} in Fig. 2(a) increases with yaw. It combines a linear variation of C_{Bx}^{ref} (Fig. 2b) and an increase followed by a decrease of C_{Rx}^{ref} (Fig. 2c). The decrease of the latter at large yaw is attributed to a thrust production on the forebody similarly to a sailing boat (Fan et al., 2022). The continuous increase of C_{Bx}^{ref} is due to a wake effect associated with three-dimensional separations along the body edges produced by the crosswind (McArthur et al., 2018).

Next Figs. 2(d, e, f) compare the drag and its contributions of the squareback geometry (denoted with superscript "0") to the reference design. It is surprising in Fig. 2(d) that it is only in a very limited yaw range of approximately $\pm 5^\circ$ that the squareback geometry has a larger drag than the reference design. For larger yaw, the squareback design is clearly better for drag than the reference design. However, Fig. 2(e) indicates that the squareback base drag C_{Bx}^0 is actually always larger than that of the reference design and gradually reaches the same value for the largest yaw. The lower drag at large yaw of the squareback is thus likely an effect localised on the rear modules consistent with the observed decrease of ΔC_{Rx}^0 in Fig. 2(f). This observation motivates the study in the next section to identify the rear designs that minimize the drag for all attitudes.

The high sensitivity of the aerodynamics with the body attitude at all pitch angles and small yaw is an effect of the steady wake instability. For the squareback design, it is known to produce a permanent asymmetry of the wake (Grandemange et al., 2012) and transitions of the wake asymmetry orientation in the (α, β) attitudes plane (Fan et al., 2022). It is observable from the base pressure gradient as reported in Fan et al. (2022) and in Fig. 3 for the attitudes explored by the squareback model in this work. At zero yaw, the mean gradient is vertical ($G_y^0 = 0$), with a sign of G_z^0 se-

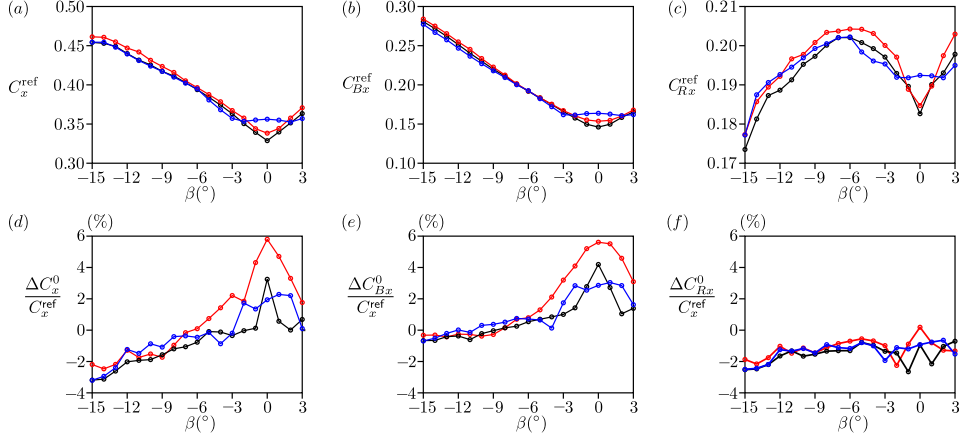


Fig. 2: Drag coefficient C_x^{ref} (a) of the reference design and its 2 contributions C_{Bx}^{ref} (b), C_{Rx}^{ref} (c) versus the body attitude (α, β). The right column shows the comparison of drag between the reference design C_x^{ref} and the squareback geometry C_x^0 ($\varphi_t = \varphi_b = 0^\circ$).

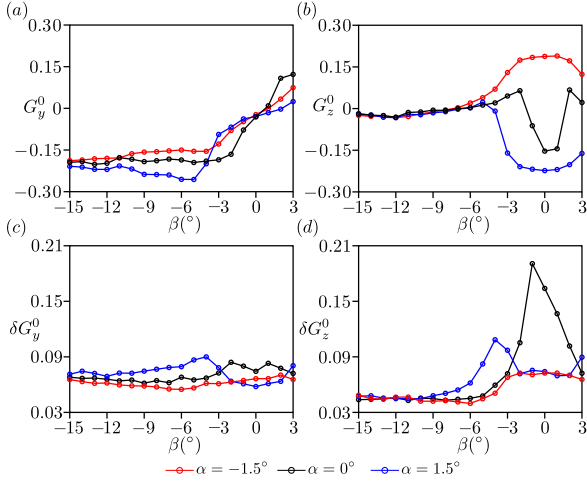


Fig. 3: Mean pressure gradient components, (a) G_y^0 , (b) G_z^0 of the squareback geometry vs. the body attitude and their corresponding fluctuation, (c) δG_y^0 and (d) δG_z^0 .

lected by the pitch value (Fig. 3a,b). At large yaw the gradient changes its orientation and becomes horizontal ($G_z^0 = 0$). These wake transitions are accompanied with large fluctuations exclusively in the vertical direction ($\delta G_z^0 > \delta G_y^0$) as can be seen in Fig. 3(c,d). With the reference design shown in Fig. 4(a,b), similar changes of the mean gradient orientation are observed with yaw and pitch. However, fluctuations in Fig. 4(c,d) are not exclusively in the vertical direction anymore. This is the case for the attitude ($0^\circ, 0^\circ$) that exhibits equivalent fluctuations in both gradient components. To conclude, the high sensitivity of the drag to pitch in

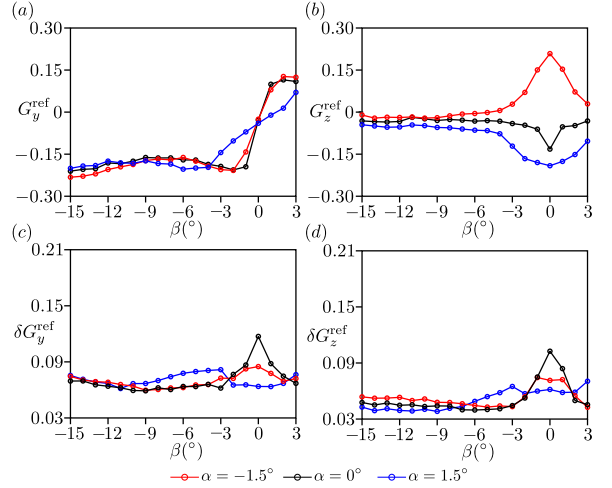


Fig. 4: Mean pressure gradient components, (a) G_y^{ref} , (b) G_z^{ref} of the reference design vs. the body attitude and their corresponding fluctuation, (c) δG_y^{ref} and (d) δG_z^{ref} .

Fig. 2(a) for the reference design is related to a wake effect as shown in Fig. 4.

4.2 Wake sensitivity to the rear design and body attitude

The wake statistical properties of all investigated rear designs and body attitudes are now analysed using the mean $G_i(\varphi_t, \varphi_b)$ and the fluctuation $\delta G_i(\varphi_t, \varphi_b)$ of the base pressure gradient components $i = y, z$.

We first look at the case $\beta = 0^\circ$ for the three pitch attitudes in Fig. 5. While the horizontal mean component in Fig. 5(a) remains almost null for all pitch angles as expected by symmetry, the vertical mean gradient in Fig. 5(b) undergoes sharp transitions between two opposite values of approximately ± 0.2 . We will respectively call the negative and positive value, the "N" and "P state" of the wake. The pitch-down attitude in Fig. 5(b, left) is associated with a *P* state which, depending on the rear design, can transition to an *N* state when the body is pitched-up in Figs. 5(b, mid, right). This was actually the case for the squareback and reference designs as previously observed in Fig. 3(b) and Fig. 4(b) respectively at $\beta = 0^\circ$. Independently to the pitch angle variation, the rear design can also trigger the transition as observed for the case $\alpha = 0^\circ$ in Fig. 5(b, mid), and pitch-up attitude in Figs. 5(b, right). All transitions, whether produced with variation of pitch attitude or rear design, can be simply related to a downwash or upwash wake effect, i.e.: a negative or positive vertical velocity in the wake. Pitching-down the body in Fig. 5(b, left) will produce an upwash effect similarly to a rear design with $\varphi_b > \varphi_t$ in Figs. 5(b, mid, right). An upwash increase is thus associated with a *P* state in all Figs. 5(b). Identically, a downwash effect, either by pitching-up the body or with a rear design such that $\varphi_t > \varphi_b$, is associated with an *N* state in all Figs. 5(b). As a rule of thumb, an *N* state of the wake is selected by increasing the downwash effect and a *P* state by increasing the upwash effect. All the transitions, indicated by $G_z = 0$ in Figs. 5(b, mid, right), are accompanied by fluctuation crisis of the gradient components in Figs. 5(c, d, mid, right) in agreement with the attitude parametric study of Fan et al. (2022) for the squareback design. The increase of the fluctuation in Figs. 5(c, d, left) towards the design (12.5°, 0°) probably announces a transition for rear designs out of the map such that $\varphi_b < 0^\circ$ and $\varphi_t > 12.5^\circ$.

In order to investigate the yaw effect on the base pressure gradient, we selected attitudes with no pitch and $\beta = -1^\circ, -3^\circ, -5^\circ$ as shown in Fig. 6. A negative horizontal component appears at $\beta = -1^\circ$ in Fig. 6(a, left) which then saturates to -0.2 (Fig. 6a, mid, right) and for all yaw angles beyond $|\beta| \geq 5^\circ$, irrespective of the rear design and pitch attitude (not shown here). Note that the same thumb rule applies between the sidewash and the base pressure gradient; the negative yaw produces a negative sidewash and a negative horizontal pressure gradient. The sharp transition

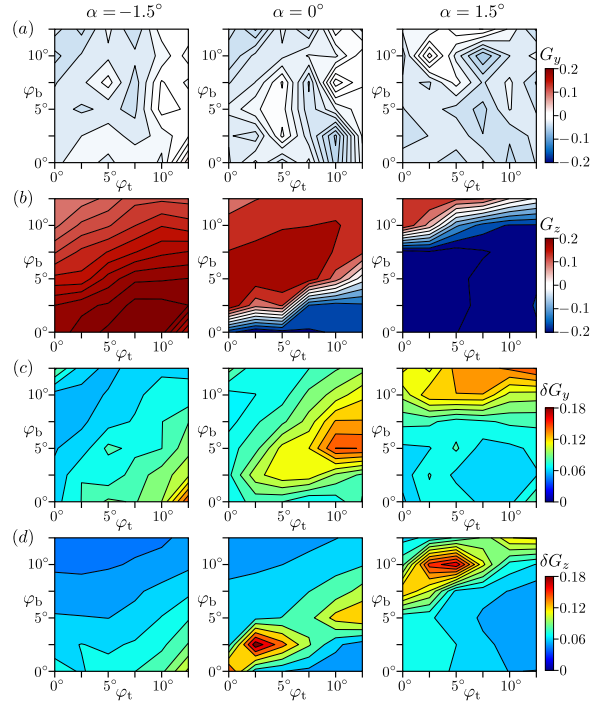


Fig. 5: Base pressure gradient as a function of the rear design (φ_t, φ_b) at $\beta = 0^\circ$ with pitch (left column) $\alpha = -1.5^\circ$, (mid column) $\alpha = 0^\circ$, (right column) $\alpha = +1.5^\circ$. Components of the mean pressure gradient (a) G_y , (b) G_z and their corresponding fluctuation (c) δG_y , (d) δG_z .

between opposite values of the vertical gradient component is still observable in Fig. 6(b, left) for rear designs of small angles only. It is replaced by a quasi-linear and low variation for increased yaw $|\beta| > 3^\circ$. Yaw angles up to $|\beta| = 15^\circ$ are not shown as they display the same map as Fig. 6(b, right). The two components of the base pressure gradient become insensitive to the yaw and pitch for $|\beta| > 3^\circ$.

4.3 Drag sensitivity to the rear design and body attitude

The previous section has shown the cumulative effect of the rear design and the attitude on a wake property given by the base pressure gradient. We are now looking at the consequence on both the base and total drag coefficient.

The base drag maps in the rear design space $C_{Bx}(\varphi_t, \varphi_b)$ are given in Fig. 7(a) for the same attitudes as for the base pressure gradient maps shown in Fig. 5. A strong correlation can be observed with the vertical component of the gradient (Fig. 5b) re-

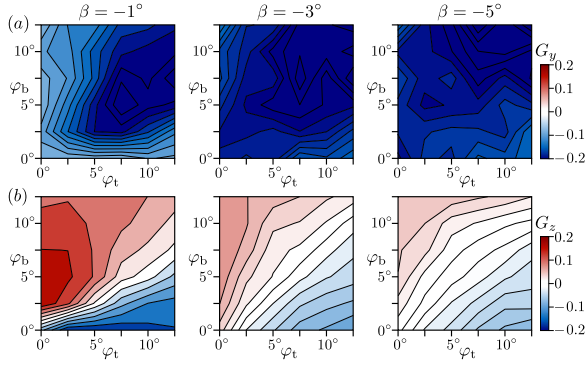


Fig. 6: Base pressure gradient as a function of the rear design (φ_t, φ_b) at $\alpha = 0^\circ$ with yaw (left column) $\beta = -1^\circ$, (mid column) $\beta = -3^\circ$, (right column) $\beta = -5^\circ$. Components of the mean pressure gradient (a) G_y , (b) G_z .

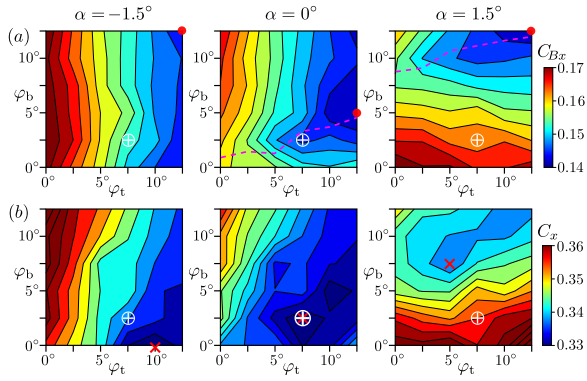


Fig. 7: Base drag (a) C_{Bx} and drag (b) C_x as function of the rear design (φ_t, φ_b) at $\beta = 0^\circ$ with pitch (left column) $\alpha = -1.5^\circ$, (mid column) $\alpha = 0^\circ$, (right column) $\alpha = +1.5^\circ$. Symbols • and x (in red) show the optimal rear designs for minimum C_{Bx} and C_x , respectively. The white symbol \oplus denotes the reference design. Labels P and N as well as the black dividing line in (a) refer to wake states and transitions from Fig. 5b.

lated to the wake transition between the P and N state identified in the previous section and marked with the red dashed line in Fig. 7(a, mid, right). When the wake is in a P state, that concerns all designs in Fig. 7(a, left), and only those above the transition line in Figs. 7(a, mid, right), the base drag iso-lines are rather vertical. It simply means that for the P state of the wake only the top angle has an authority on the base drag. When the wake is in the N state, that concerns designs below the transition line in Figs. 7(a, mid, right), the base drag iso-lines are rather horizontal. In the N

state, the authority on the base drag is due to the bottom angle. It indicates that for these three pitch attitudes, the base drag is actually controlled by the angle located on the high pressure hand side of the base. For the two pitch angles where the design variation produces the wake transition (Fig. 5a, mid, right), the minimum base drag is obtained at the transition and for the largest angles. The correlation of the total drag maps in Figs. 7(b) with the base pressure gradient are less obvious (but still observable) because of the contribution of the rear design, i.e., the force acting on the slanted surfaces before the trailing edge flow separation. As a consequence, the minimum drag is obtained for different rear designs having lower angle values than those with minimum base drag.

The drag sensitivity to pitch is reduced at yaw as can be seen for $\beta = -8^\circ$ in Fig. 8 and $\beta = -13^\circ$ in Fig. 9 for which all maps are quite similar. At large yaw, the minimum drag is observed for the squareback design ($\varphi_t = \varphi_b = 0^\circ$), indicating that the introduction of tapers produces drag increase.

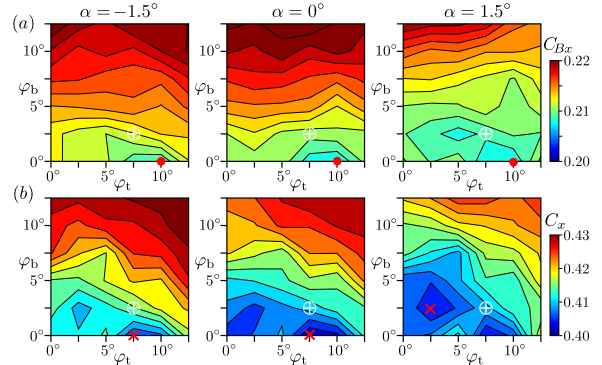


Fig. 8: Base drag (a) C_{Bx} and drag (b) C_x as a function of the rear design (φ_t, φ_b) at $\beta = -8^\circ$ with pitch (left column) $\alpha = -1.5^\circ$, (mid column) $\alpha = 0^\circ$, (right column) $\alpha = 1.5^\circ$. The red cross and filled circle symbols show the optimal rear design for minimum drag and base drag respectively.

The design that minimises the wind-averaged drag coefficient defined in Eq. 9 can be found from Fig. 10, which maps the wind-averaged drag C_{DWC} for the 3 pitch attitudes in the rear design space. The wind-averaged optimal design is very different at the positive pitch to that at the zero and negative pitch. A larger drag reduction at all pitch angles would require a rear design that

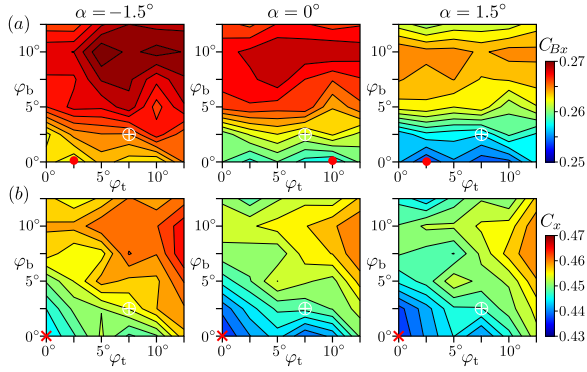


Fig. 9: Same caption as for Fig. 8 but at $\beta = -13^\circ$.

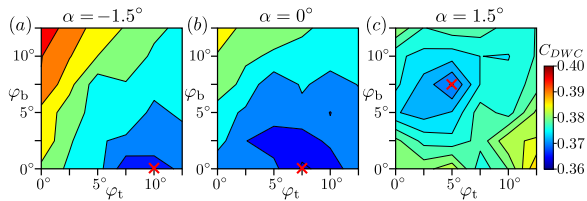


Fig. 10: The wind-averaged drag C_{DWC} as a function of the rear design (φ_t, φ_b) at different pitch attitudes: (a) $\alpha = -1.5^\circ$; (b) $\alpha = 0^\circ$; (c) $\alpha = +1.5^\circ$;

adapts to the body attitude as investigated in the following section.

4.4 Adaptive rear design

We address in this section the question of what improvements can be achieved if the design could adapt to the best rear couple of angles that makes the total drag coefficient the lowest each time the body attitude changes. Strictly speaking there is no adaptive control here, but optimal designs can be selected from all the investigated attitudes and rear designs to answer the question.

Optimal designs that minimize the drag denoted $(\varphi_t^{\text{opt}C_x}, \varphi_b^{\text{opt}C_x})$ or the base drag denoted $(\varphi_t^{\text{opt}C_{Bx}}, \varphi_b^{\text{opt}C_{Bx}})$ for the 57 different attitudes are shown in Fig.11. Except for the 3 attitudes favoring the $(5^\circ, 7.5^\circ)$ design in Fig. 11(a), to which we will return later, the optimal drag designs mainly concentrate on a range with small bottom angles ($\varphi_b^{\text{opt}C_x} \leq 2.5^\circ$). In contrast, the optimal base drag designs that minimises base drag in Fig. 11(b) appear over a wider region with $\varphi_t^{\text{opt}C_{Bx}} \geq \varphi_b^{\text{opt}C_{Bx}}$ involving larger angles. The discrepancy between the optimal configurations in drag and base drag confirms the additional drag on the slanted sur-

faces that neutralizes the drag reduction obtained with the pressure recovery of the thinner wake resulting from larger angles rear design (Wong and Mair, 1983). We have grouped in Fig. 11 with a pink area all optimal designs for yaw $|\beta| \leq 2^\circ$, blue for yaw in the range $12^\circ \geq |\beta| \geq 2^\circ$, and green for yaw $|\beta| \geq 12^\circ$. These three regions will be called A, B and C.

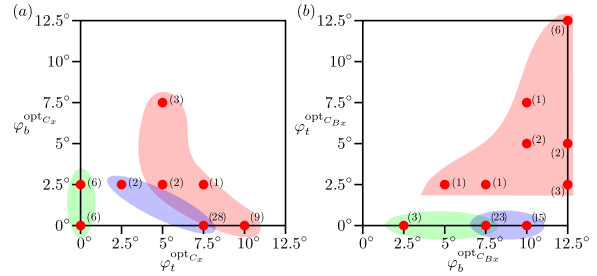


Fig. 11: Overview of all optimal designs that minimise (a) drag and (b) base drag for the 57 different body attitudes, values in bracket represent the number of occurrences. Coloured areas A, B and C group respectively optimal designs in the yaw ranges: $|\beta| \leq 2^\circ$ for pink, $12^\circ \geq |\beta| \geq 2^\circ$ for blue, and $|\beta| \geq 12^\circ$ for green.

The drag variation and its contributions of the optimal designs $(\varphi_t^{\text{opt}C_x}, \varphi_b^{\text{opt}C_x})$ from the reference design obtained at each attitude are shown in Figs. 12. We can see that the 3 regions A, B and C show very distinctive variations in Fig. 12(a).

The pitch sensitive domain corresponds to region A where a maximum drag reduction of 3% to 5% is achieved for the pitch-down and pitch-up attitude respectively. As said above, from the base pressure gradient observation in Fig. 5, there is a wake effect subjected to the steady instability sensitive to both the pitch and the rear design, of which the pressure recovery in the recirculating flow reduces both the base drag in Fig.12(b) and the rear design drag in Fig.12(c). The far-off design $(5^\circ, 7.5^\circ)$ previously mentioned in Fig. 11(a) actually corresponds to the 3 attitudes with nose-up pitch at $\beta = -1^\circ, 0^\circ, +1^\circ$ having the largest drag reduction in region A of Fig. 12(a). At these nose-up attitudes, the reference design selects an N state as can be seen in Fig. 7(right) that is a high base drag configuration. The minimum base drag is obtained for the

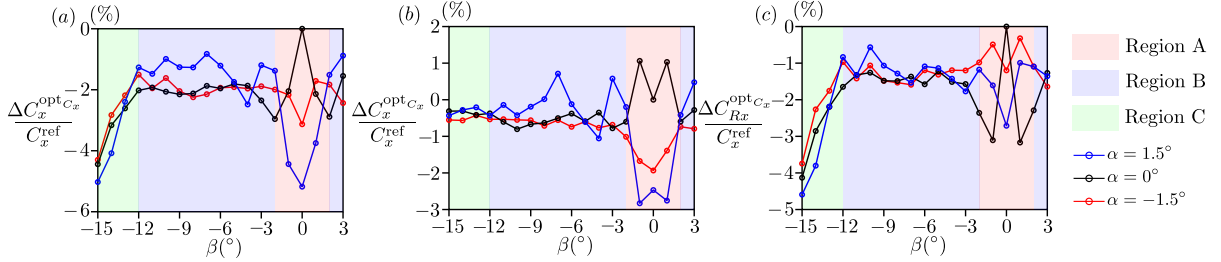


Fig. 12: Relative difference to the reference design in percent of (a) drag, (b) base drag and (c) remaining drag of the optimal designs that minimizes the drag vs. the body attitude.

Table 1: Drag for the different rear designs at different attitudes.

| Rear design (φ_t, φ_b) | C_x at $\beta = 0^\circ$ | | | C_{DWC} | | |
|---|----------------------------|--------------------|----------------------|-----------------------|--------------------|----------------------|
| | $\alpha = -1.5^\circ$ | $\alpha = 0^\circ$ | $\alpha = 1.5^\circ$ | $\alpha = -1.5^\circ$ | $\alpha = 0^\circ$ | $\alpha = 1.5^\circ$ |
| Squareback ($0^\circ, 0^\circ$) | +5.9% | +3.3% | +2.0% | +3.0% | +1.4% | +0.8% |
| Reference ($7.5^\circ, 2.5^\circ$) | 0.338 | 0.329 | 0.356 | 0.369 | 0.362 | 0.375 |
| Optimal wind-averaged ($7.5^\circ, 0^\circ$) | -2.1% | +0.6% | +0.8% | -1.9% | -0.6% | -0.3% |
| Adaptive ($\varphi_t^{\text{opt}C_x}, \varphi_b^{\text{opt}C_x}$) | -3% | 0% | -5.1% | -2.4% | -0.8% | -3.2% |
| Adaptive ($\varphi_t^{\text{opt}C_{Bx}}, \varphi_b^{\text{opt}C_{Bx}}$) | -0.3% | +0.6% | -4.5% | -1.1% | -0.6% | -2.9% |

design ($12.5^\circ, 12.5^\circ$) in Fig. 7(a, right) that introduces the P state in the dynamics resulting in a zero mean vertical base pressure gradient component and large fluctuations (Fig. 5b, c, d, right). However, it is compromised by the additional drag on the slanted surface, leading to the optimal design ($5^\circ, 7.5^\circ$) with smaller tapers angles for minimal drag. Compared to the reference and wind-averaged static designs whose drag coefficients are summarized in Table 1, the adaptive design that minimises the drag presents a clear improvement for pitch attitude variations at zero yaw. The table also shows the drag reduction obtained with an adaptive design that minimises the base drag. For practical reasons, drag is not accessible on real road conditions while base drag can be correctly assessed with only few pressure measurements. It still produces a clear improvement at the positive attitude because of the wake effect and its underlying steady instability.

Moderate yaw angles of the region B in Fig.12(a) show constant drag reduction of about 2% until $\beta = -12^\circ$. This drag reduction is approximately half of base drag reduction (Fig.12b) and half of slanted surface drag reduction (Fig.12c).

At larger yaw ($|\beta| \geq 12^\circ$), an increasing trend for drag reduction up to 5% is observed in region C in Fig.12(a), while the base drag reduction is approximately 0.5% in Fig.12(b). This considerable drag reduction is exclusively due to the pressure recovery on the rear design as can be seen in Fig.12(c). Basically, the drag reduction is obtained

by the adaptive removal of the tapers angle, that is efficient at small yaw to reduce drag but clearly detrimental at large yaw.

Table 1 recaps the wind-aligned (C_x) and wind-averaged (C_{DWC}) drag properties of the model with different rear designs. The wind-averaged drag coefficient shows a clear sensitivity to pitch. The optimal rear design based on the wind-averaged drag at zero pitch ($\varphi_t = 7.5^\circ, \varphi_b = 0^\circ$) is obtained from the minimum in Fig. 10(b). While this design has slightly worse performance for zero and positive pitch in wind-aligned conditions, it produces a global improvement for the C_{DWC} value for all pitch attitudes; a reduction of 1.9% is observed for the negative pitch, while it remains below 1% for the two other pitch angles. Adaptive rear design, optimized versus the total drag, demonstrates clear advantages with respect to the reference and optimal wind-averaged rear designs. Total drag is reduced by up to 5.1% in wind-aligned, and 3.2% in wind-averaged conditions for a positive pitch angle, and 3% and 2.4%, respectively for a negative pitch angle. The optimisation of the rear design with respect to the base drag only also leads to interesting improvements.

5 Conclusion

We have studied the drag reduction of a taller-than-wide squareback Ahmed body by modifying its rear design with top and bottom tapers of an-

gles in the range $[0^\circ, 12.5^\circ]$. The effect of the rear design was investigated at yaw up to 15° and for 3 pitch attitudes ; $\pm 1.5^\circ$ and 0° . All drag reduction in % were calculated from the reference design, having the lowest drag in aligned flow condition. The wake, shown to be subjected to the steady wake instability in the vertical direction, is highly sensitive to the body attitude and rear design particularly at yaw smaller than 2° where the study leads to the following conclusions :

- The high sensitivity is a consequence of the difference between the only two possible vertical asymmetries (the P and N states) of the steady wake instability.
- A small change of the vertical perturbation velocity induced by the rear design and/or the body pitch is able to reverse the vertical asymmetry of the wake. It is found that a wake in the P state (positive base pressure gradient) requires additional downwash effect (or a negative vertical velocity) to produce a reversal towards the N state and conversely, a wake in the N state requires additional upwash effect (or a positive vertical velocity) to produce a reversal towards the N state. On the practical point of view, small changes in the rear design can control the wake state when the pitch of the model varies and for yaws smaller than 3° .
- The top and bottom tapers do not have an equivalent authority to change the base drag. It is found that when the wake is in a P state, the bottom taper has no effect on the base pressure while the top one is able to decrease the base drag as its angle increases. Inversely for a wake in the N state, only the bottom spoiler decreases the base drag as its angle increases. This result indicates that only the taper located on the high pressure side of the base has the authority to change the base drag. This interesting result related to the existence of the steady instability deserves further investigation to be fully understood.

Adaptive rear designs for these attitudes improve drag reduction up to 5% compared to the reference design. It is explained by the ability of the rear design to control the wake state when the pitch varies. It produces a dominant impact on the base pressure.

For yaws larger to 2° and up to 12° , the sensitivity to pitch reduces, essentially because the wake asymmetry becomes horizontal. Compared to the reference design, adaptive tapers achieve about 2% drag reduction. The dominant contribution for

the reduction is identified as the drag on the tapers.

For yaws larger than 12° , a substantial reduction of 5% is obtained with adaptive tapers compared to the reference design. This effect has no contribution from the pressure at the base, it is exclusively due to the drag on the tapers that reduces by decreasing their angle to zero as the yaw increases. The best design at large yaw is then the squareback geometry. This result motivates the exploration of negative angle for tapers at large yaws.

Overall, compared to the rear reference static design having a minimum drag at zero attitude, the adaptive rear design can achieve up to 3.2% reduction of the wind-averaged drag coefficient which takes into account crosswind effects. Top and bottom rear tapers show an efficiency in crosswind to reduce drag that is comparable to the side tapering of [Garcia de la Cruz et al. \(2017\)](#). Drag reduction should be further increased with tapers at the four trailing edges of the base ([Urquhart et al., 2020b](#); [Varney et al., 2018](#)). It motivates our future perspective to implement a morphing afterbody with a closed-loop control strategy for the drag mitigation.

Acknowledgements The authors would like to acknowledge the invaluable contributions of both the mechanical and electrical workshops of the University of Liverpool to set-up the experiment. Y. F. wishes to thank the China Scholarship Council (CSC No. 202006260028) for the doctoral financial support. This work has been supported by the Khalifa University of Science, Technology and Research under Award No. CIRA-2019-025.

Declarations

Ethical Approval

not applicable

Competing interests

The authors declare that they have no conflict of interest

Authors' contributions

Y.F. and O.C. produced the results. All authors analysed the results. Y.F. prepared all figures and a first draft. Y.F, O.C. and V.P. wrote the final version. All authors reviewed the manuscript.

Funding

This work has been supported by the Khalifa University of Science, Technology and Research under Award No. CIRA-2019-025.

Availability of data and materials

on request to the authors

References

- Ahmed S, Ramm G, Faitin G (1984) Some salient features of the time-averaged ground vehicle wake. SAE Technical Paper Series 840300
- Bello-Millán F, Mäkelä T, Parras L, del Pino C, Ferrera C (2016) Experimental study on ahmed's body drag coefficient for different yaw angles. *Journal of Wind Engineering and Industrial Aerodynamics* 157:140–144
- Bonnaivon G, Cadot O, Évrard A, Herbert V, Parpais S, Vigneron R, Détery J (2017) On multistabilities of real car's wake. *Journal of Wind Engineering and Industrial Aerodynamics* 164:22–33
- Bonnaivon G, Cadot O, Herbert V, Parpais S, Vigneron R, Détery J (2019) Asymmetry and global instability of real minivans' wake. *Journal of Wind Engineering and Industrial Aerodynamics* 184:77–89
- Cooper K (1976) Wind tunnel investigation into the fuel savings available from the aerodynamic drag reduction of trucks. *Natl Res Counc Can Div Mech Eng Q Bull* (3):31 – 87
- Garcia de la Cruz JM, Brackston RD, Morrison JF (2017) Adaptive base-flaps under variable crosswind. In: SAE Technical Paper Series, SAE International, vol 2017-01-7000
- Evstafyeva O, Morgans AS, Dalla Longa L (2017) Simulation and feedback control of the ahmed body flow exhibiting symmetry breaking behaviour. *Journal of Fluid Mechanics* 817:R
- Fan Y, Parezanović V, Cadot O (2022) Wake transitions and steady z-instability of an ahmed body in varying flow conditions. *Journal of Fluid Mechanics* 942:A22
- Gohlke M, Beaudoin J, Amielh M, Anselmet F (2007) Experimental analysis of flow structures and forces on a three-dimensional bluff body in constant cross-wind. *Experiments in Fluids* 43(4):579–594
- Grandemange M, Gohlke M, Cadot O (2012) Reflectional symmetry breaking of the separated flow over three-dimensional bluff bodies. *Physical Review E* 86:035302
- Grandemange M, Gohlke M, Cadot O (2013a) Bi-stability in the turbulent wake past parallel-piped bodies with various aspect ratios and wall effects. *Physics of Fluids* 25:95–103
- Grandemange M, Gohlke M, Cadot O (2013b) Turbulent wake past a three-dimensional blunt body. Part 1. Global modes and bi-stability. *Journal of Fluid Mechanics* 722:51–84
- Grandemange M, Mary A, Gohlke M, Cadot O (2013c) Effect on drag of the flow orientation at the base separation of a simplified blunt road vehicle. *Experiments in fluids* 54(5):1–10
- Grandemange M, Cadot O, Courbois A, Herbert V, Ricot D, Ruiz T, Vigneron R (2015) A study of wake effects on the drag of the Ahmed square-back model at the industrial scale. *Journal of Wind Engineering and Industrial Aerodynamics* 145:282–291
- Hassaan M, Badlani D, Nazarinia M (2018) On the effect of boat-tails on a simplified heavy vehicle geometry under crosswinds. *Journal of Wind Engineering and Industrial Aerodynamics* 183:172–186
- Howell J (2015) Aerodynamic drag of passenger cars at yaw. *SAE International Journal of Passenger Cars-Mechanical Systems* 8(2015-01-1559):306–316
- Howell J, Passmore M, Windsor S (2018) A drag coefficient for test cycle application. *SAE International Journal of Passenger Cars-Mechanical Systems* 11(5):447–461
- Ingram K (1978) Wind-averaged drag coefficient applied to heavy goods vehicles. *TRRL Suppl Rep* (392)
- Littlewood R, Passmore M (2010) The optimization of roof trailing edge geometry of a simple squareback. SAE Technical Paper Series 2010-01-0510
- McArthur D, Burton D, Thompson M, Sheridan J (2018) An experimental characterisation of the wake of a detailed heavy vehicle in crosswind. *Journal of Wind Engineering and Industrial Aerodynamics* 175:364–375
- Meile W, Ladinek T, Brenn G, Reppenhagen A, Fuchs A (2016) Non-symmetric bi-stable flow around the Ahmed body. *International Journal of Heat and Fluid Flow* 57:34–47
- Perry A, Pavia G, Passmore M (2016) Influence of short rear end tapers on the wake of a simplified square-back vehicle: wake topology and rear drag. *Experiments in Fluids* 57(11):169
- Perry AK, Passmore M, Finney A (2015) Influence of short rear end tapers on the base pressure of a simplified vehicle. *SAE International Journal of Passenger Cars - Mechanical Systems* 8(1):317–327

- Urquhart M, Ljungskog E, Sebben S (2020a) Surrogate-based optimisation using adaptively scaled radial basis functions. *Applied Soft Computing Journal* 88
- Urquhart M, Varney M, Sebben S, Passmore M (2020b) Aerodynamic drag improvements on a square-back vehicle at yaw using a tapered cavity and asymmetric flaps. *International Journal of Heat and Fluid Flow* 86
- Varney M, Passmore M, Gaylard A (2018) Parametric study of asymmetric side tapering in constant cross wind conditions. *SAE International Journal of Passenger Cars - Mechanical Systems* 11
- Wong DM, Mair W (1983) Boat-tailed afterbodies of square section as drag-reduction devices. *Journal of Wind Engineering and Industrial Aerodynamics* 12(2):229 – 235
- Zampogna G, Boujo E (2023) Linear and weakly nonlinear stability of rectangular prisms. *J Fluid Mech* 966:A19